Journal of Magnetics 8(1), 36-44 (2003)

Recent Development of MRAM Technology

T. Miyazaki*, Y. Ando and H. Kubota

Department of Applied Physics, Graduate School of Engineering, Tohoku University, Sendai 980-8579, Japan

(Received 10 December 2002)

Three topics which are related to technologies for developing of large capacity MRAM over Gbits are reviewed. First, it is stressed that inelastic-electron-tunnel-tunneling spectroscopy (IETS) is a powerfull method to investigate the interface state between magnetic electrodes and insulator. Second, magnetic tunnel junctions with small bias voltage dependence are introduced. Finally, fabrication method of carbon masks for very small magnetic tunnel junctions is demonstrated. These three topics were presented at 47th MMM 2002 conference and each paper will appear in the proceedings.

Key words : MRAM, magnetic tunneling junction, non volatile memory, tunneling spectroscopy

1. Introduction

Magnetoresistive Random Access Memory (MRAM) has a great potential to replace other memories which have been used in various electronic systems. Key attributes of MRAM technology are non volatility, unlimited read and write endurance and high speed operation. Many companies have an interest in developing large capacity MRAM and 1 Mbits MRAM have been already reported by Motorola group. If we want to develop larger capacity MRAM over Gbits, (1) high out put voltage, (2) high speed, (3) low power consumption and (4) high reliability are required. In order to investigate such tunnel junctions which satisfies above requirements, evaluation of the tunnel conductivity in magnetic tunnel junction is very useful. A study to develop a junction with high TMR ratio and low bias dependence is particularly important. Technologies such as micro-fabrication and stacking are indespensable for high density and large capacity MRAM. In this paper three topics being investigated in our group will be introduced. Namely, interface characterization of magnetic tunnel junctions by using tunneling spectroscopy, fabrication of magnetic tunnel junctions with small bias voltage dependence and hard mask fabrication for MRAM elements using focused ion beam.

*Corresponding author: Tel: +81-22-217-7946, e-mail: miyazaki@mlab.apph.tohoku.ac.kr

2. Interface characterization of magnetic tunnel junctions by using tunneling spectroscopy

Since large tunnel magnetoresistance (TMR) at room temperature was observed [1, 2], properties of magnetic tunnel junctions (MTJs) have been steadily improved. Especially since very large TMR ratios of more than 40% were reported by several groups [3-5] it is believed that devices based on the TMR phenomenon will become commercially viable within a few years [6]. Magnetic random access memory (MRAM) is one of the most realistic targets to be developed. In spite of the large TMR effect at low bias-voltage, the TMR ratio decreases with increasing the bias-voltage; therefore, improvement of the bias-voltage dependence is required. Some possible origins of the bias-dependence of TMR have been proposed [7, 8]. Magnons at the interface between ferromagnetic electrodes and the insulator induce the inelastic conduction pass with spin-flip; the TMR ratio decreases over the voltage at which the inelastic conduction pass opens. We reported on the measurements of conductive properties for magnetic tunnel junctions using inelastic-electron-tunneling spectroscopy (IETS) [9, 10]. The spin-dependent excitation at ferromagnetic electrodes was successfully observed in the spectra; therefore, this technique is useful for the interface characterization of tunnel junctions. In our recent experiment, the surface of plasma-oxidized Al had a reconstruction structure and Al termination was favored [11, 12]. Direct Al-FM (ferromagnet) bonding

must play an important role for the high positive spin polarization [13, 14]. In this work we prepared the junction doped with a little amount of Al between the top ferromagnetic electrode and the insulator. This article describes the IET spectra for the parallel (P) and anti-parallel (AP) magnetization configurations of the both ferromagnetic electrodes in order to compare with the bias-dependence of TMR ratio at low voltage region.

2.1. Experimental Procedure

Magnetic tunnel junctions were prepared by magnetron sputtering with inductively coupled plasma (ICP) onto thermally oxidized Si substrates. The stacking structure was SiO_2/Pt(3 nm)/$Ni_{80}Fe_{20}$(3 nm)/Cu(20 nm)/$Ni_{80}Fe_{20}$(3 nm)/IrMn(10 nm)/$Co_{75}Fe_{25}$ (5 nm)/Al(2 nm)-oxide/Al(d_{Al} nm)/$Co_{75}Fe_{25}$(5 nm)/$Ni_{80}Fe_{20}$(20 nm)/Pt(5 nm). The base pressure was below 2×10^{-6} Pa and sputtering was carried out in an atmosphere of 0.15 Pa Ar. The surface of 2 nm Al layer was oxidized by ICP in a mixed atmosphere of 0.75 Pa O_2 and 0.25 Pa Ar for 270 s. After the oxidation, metallic Al was fabricated on the Al-oxide layer. The junction area was $100 \times 100\ \mu m^2$ using contact metal mask. The d*I*/d*V*-*V* curves and IET spectra, *i.e.* the derivative of conductance, were measured by a modulation method using a homemade electrical circuit. In addition to a dc voltage sweep, an ac modulation voltage of 0.5~2.0 mV with a frequency of 7.8 kHz was applied to the junction. The first- and second-harmonic signals were detected simultaneously using a lock-in amplifier. Positive bias voltage was defined as the current direction from the bottom to top electrode. These measurements were performed in a magnetic field up to 100 Oe at 4.2 K.

2.2. Results and Discussion

Fig. 1 shows the doped Al-thickness (d_{Al}) dependences of the TMR ratio and the resistance. For the as-prepared junction, the TMR ratio decreases with increasing d_{Al}, while the resistance is almost constant; suggesting the doped Al can be metallic and the tunnel barrier thickness does not change. The TMR ratio for the junction with d_{Al} of 0.2 nm scattered. On the other hand, the TMR ratio for the annealed junction improves and has a peak at d_{Al} of 0.2 nm without the scattering. With further increasing the d_{Al} the TMR ratio decreases drastically and the resistance increases monotonically. This suggests that the Al on the insulator is oxidized by the diffusion of oxygen and form an insulator.

The second derivatives of the *I*-*V* curves (IET spectra) were measured for all junctions. A typical phonon peak of Al-O LO mode (120 mV) was observed clearly for all junctions, suggesting that inelastic electron tunneling

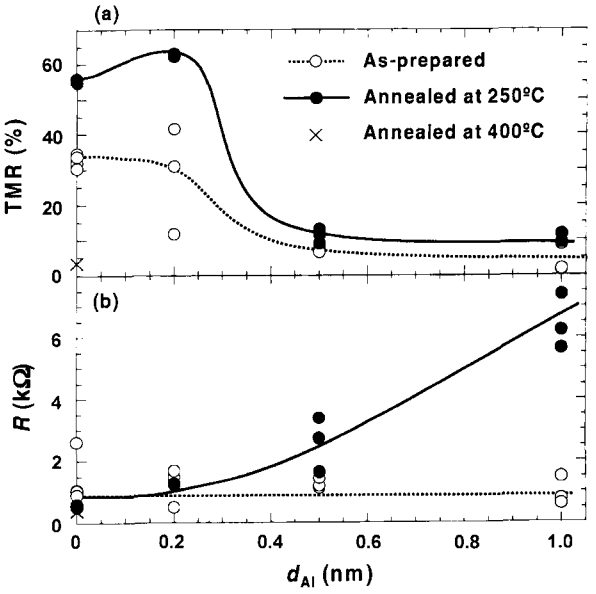

Fig. 1. (a) The TMR ratio and (b) the junction resistance at 4.2 K as a function of inserted Al thickness d_{Al}. Open circles (○), solid circles (●) and cross marks (×) indicate the data for the junctions as-prepared, annealed at 250°C and 400°C, respectively.

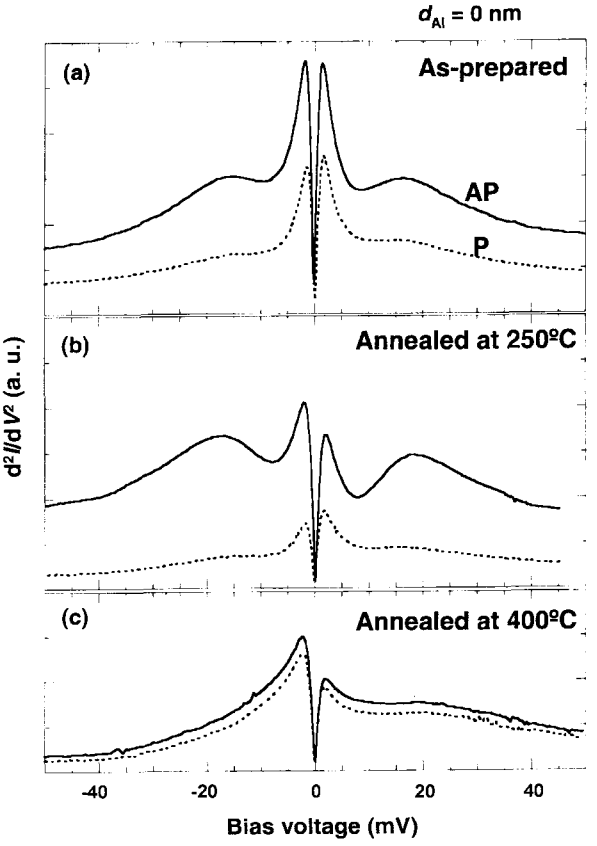

Fig. 2. The IET spectra for the P (dashed line) and AP (solid line) magnetization configurations for the tunnel junction (a) as-prepared, (b) annealed at 250°C and (c) 400°C.

currents were successfully detected in this experiment. Fig. 2 shows the IET spectra for the junctions with d_{Al} of 0 nm (a) as prepared, (b) with annealing at 250°C and (c) 400°C. Solid lines and dotted lines are the spectra of antiparallel (AP) and parallel (P) magnetization configurations. For the as-prepared junction, a sharp peak appears below 2 mV of bias voltage; it is due to zero-bias anomaly coming from magnetic impurities. A peak around 20 mV for the IET spectrum for AP configuration is characteristic; the peak disappears for the spectrum for P configuration. For the 250°C annealed junction, the peak intensity at 2 mV in both configurations decreases. It can be explained as the decrease of impurities at the interface between the ferromagnetic electrode and the insulator. The spectrum for P configuration is weak, resulting large difference between both configurations. The peak around 20 mV for AP configuration becomes clear. After annealing at 400°C, the peak around 20 mV in AP configuration disappears and the difference between both configurations becomes very small. It should be noted that the spectra for AP configuration are larger than those for P configuration and that these spectra are asymmetric with respect to the bias directions. As a spin-independent process does not affect the IET spectrum by applying an external magnetic field, the difference between the spectra for the P and AP configurations is expected to be only due to spin-dependent processes. For one of them, magnon-assisted inelastic tunneling currents for the P and AP magnetization configurations can be expressed [7] as

$$I_P=\frac{2\pi e}{\hbar}\sum_{\alpha} X^{\alpha} g_{\downarrow}^{L} g_{\uparrow}^{R}\int d\omega \rho_{\alpha}^{mag}(\omega)(eV-\omega)\theta(eV-\omega) \quad (1)$$

$$I_{AP}=\frac{2\pi e}{\hbar}[X^{\alpha} g_{\uparrow}^{L} g_{\uparrow}^{R}\int d\omega \rho_{R}^{mag}(\omega)(eV-\omega)\theta(eV-\omega),$$

$$+[X^{L} g_{\downarrow}^{L} g_{\downarrow}^{R}\int d\omega \rho_{R}^{mag}(\omega)(eV-\omega)\theta(eV-\omega)] \quad (2)$$

where X is the incoherent tunnel exchange vertex, $\rho_{\beta}^{mag}(\omega)$ is the magnon density of states, $g^{L(R)}$ marks the corresponding electron density of states on the left (right) electrode, $\theta(x)$ is the step function, $\alpha = L, R$. These equations can be extended to the currents by all spin-dependent inelastic processes. The first term in Eq. (2) for the AP configuration can be dominant because $g_{\uparrow}^{L} g_{\uparrow}^{R}$ is much larger than $g_{\downarrow}^{L} g_{\downarrow}^{R}$ and $g_{\downarrow}^{L} g_{\uparrow}^{R}$. Therefore, the IET spectrum for the AP configuration is normally large and more sensitive to the spin-dependent scattering at R electrode. In this experiment, electrons flow into the bottom electrode when positive bias voltage is applied, in other words R means the bottom electrode at positive bias; the peak intensity at positive bias voltage reflects the density of states of the spin-scattering modes at the bottom electrode. When P or AP alignment in the junction is improved, the difference between the spectra of both configurations becomes large. After annealing at 250°C, the squareness of the magnetoresistance loop was improved: it is due to the improvement of both the <111> orientation of the pinning layer and the interface structure [15]. As the result the separation between both spectra becomes clear. Disappearance of the peak at 20 mV after annealing at 400°C might relate to the decrease of spin polarization of the ferromagnetic electrodes.

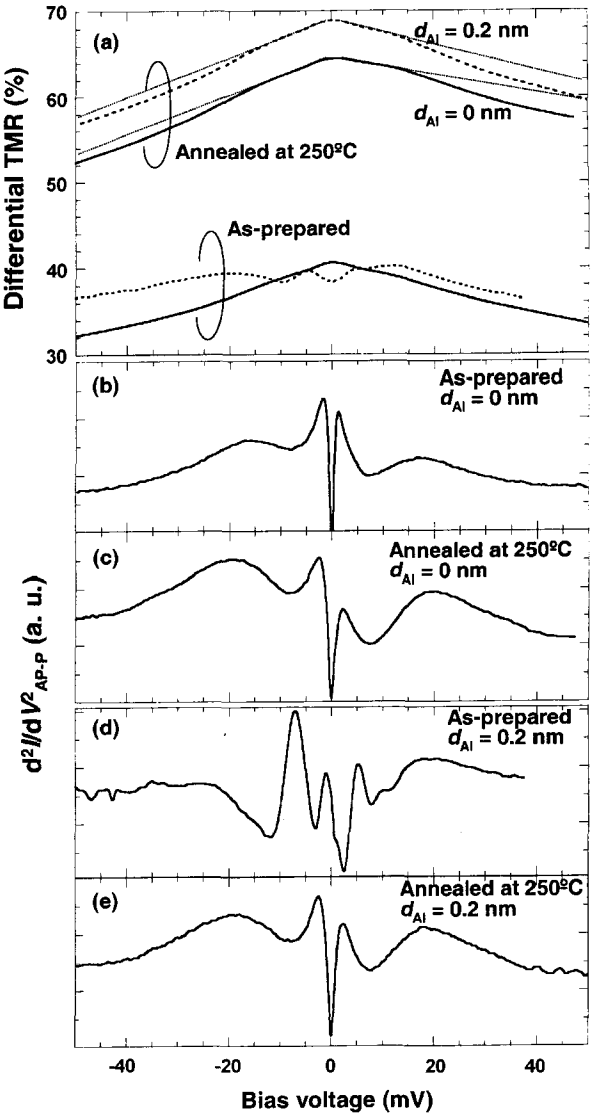

Fig. 3. The bias voltage dependence of (a) the differential TMR ratio for the tunnel junctions of both magnetization configurations and the corresponding subtracting IET spectra for the junction with d_{Al} of 0 nm (b), (c) and those with d_{Al} of 0.2 nm (d), (e). Both spectra for the junction as-prepared and annealed at 250°C are indicated.

By subtracting the IET spectrum at P configuration from that at AP configuration, we can eliminate terms due to both the spin-independent excitation and imperfect

configuration. Here, we discuss the relationship between the spin-dependent excitation and the TMR ratio as a function of the bias voltage for the junctions with $d_{Al} = 0$ and 0.2 nm. Fig. 3 shows (a) the bias dependence of the differential TMR ratio for the tunnel junctions of both magnetization configurations and (b)-(e) the corresponding subtracting IET spectra. Here, the differential TMR was obtained from the d*I*/d*V*-*V* measured simultaneously with the IET spectra. For the junction with d_{Al} of 0.2 nm as prepared (d), the IET spectrum is very complicated especially around zero-bias. The shape of the spectrum changes for every sample despite of the same stacking structure. This suggests that the Al deposited on insulator is unstable for as-prepared state and it behaves as a large number of impurities. On the other hand, the IET spectrum after annealing at 250°C (e) becomes stable and similar to that for the junction with $d_{Al} = 0$. It can be due to the formation of the stable insulator by diffusing of the Al and oxygen. The TMR ratio for the junction with d_{Al} of 0.2 nm after annealing is constantly large in comparison with the junction with $d_{Al} = 0$. This can be due to the change of the density of states (DOS) at the interface; resulting the change of the spin-polarization. Some calculations suggested that the termination of Al-Co (or Fe) had an important role in the high positive spin-polarization of the tunnel junctions [13, 14]. The doping of Al at the interface by design may accelerate the Al ñ FM termination. As shown in Fig. 3 (a) by dotted lines, the TMR ratio as a function of the bias voltage deviates from the extrapolation of the bias dependence below 20 mV at which the IET spectrum shows a peak. Namely, one of the origins of the decrease of TMR ratio as a function of bias voltage is the inelastic scattering at the interface. However the influence is relatively small in comparison of intrinsic decrease; the rough estimation of the decreasing fraction is less than 10% at most. The origin of the peak around 20 mV in IET spectra is not yet clear. It is easily accepted that magnon excitation has an effect on the spectra; meanwhile, phonon contribution could be considered. It is suggested that the electron-phonon interaction can change their spin states [16]. In the calculation of the Al phonon contribution to the spectrum, transverse phonon modes with spin flip exist around the energy of 20 meV. The separation of these contributions might be possible after measuring the spectra of junctions with different phonon modes.

In summary, junctions doped a little mount of Al between the top ferromagnetic electrode and the insulator were fabricated. The TMR ratio increased at d_{Al} of 0.2 nm after annealing at 250°C. It might be the evidence that the Al-FM termination at the interface between ferromagnetic electrodes and an insulator is important for the high TMR ratio. The IET spectra have revealed the improvement of the interface after annealing. A peak around 20 mV was sensitive to the spin scattering; therefore, the clarification of the origin of the peak will be the key to improve the bias voltage dependence of the TMR ratio.

3. Magnetic tunnel junctions with high magnetoresistance and small bias voltage dependence using epitaxial NiFe(111) ferromagnetic bottom electrodes

Polycrystalline ferromagnetic (FM) films with an fcc (111) preferred orientation have been used often as bottom electrodes in magnetic tunnel junctions (MTJs). Previous works have shown that initial plasma oxidation of a thin Al film progresses through grain boundaries [17, 18]. Inhomogeneity of the insulating layer can be one reason for the decrease of tunnel magnetoresistance (TMR) ratio with increasing bias voltage. This is fatal in development of MRAM with large capacity of Gbit order. Insulating properties of Al-O thin film prepared on a single crystalline or epitaxial FM electrode probably differ from those of Al-O thin film prepared on a polycrystalline FM electrode. Recently, high quality MTJs with single crystalline or epitaxial FM electrodes were successfully fabricated [19, 20]. In this study, MTJs are fabricated using Al-O insulating layers prepared on an epitaxial $Ni_{80}Fe_{20}$ (NiFe) bottom electrode and on a polycrystalline NiFe bottom electrode. Differences in TMR ratios and their bias dependences are discussed.

3.1. Experiments

It was reported that NiFe(111) film on Si(111) substrate/Ag(111) 100 nm/Cu(111) 50 nm multilayer grew epitaxially by sputter at room temperature [21]. We adopted and modified this film structure as a buffer layer for an epitaxial NiFe layer. A Si(111) substrate was etched by NH_4F solution to remove the native oxide layer for growth of an epitaxial bottom electrode. The multilayer of Si(111)/Ag 3 nm/Cu 50 nm/NiFe 50 nm/Al-O/$Co_{75}Fe_{25}$ 4 nm/IrMn 20 nm/NiFe 20 nm/Ta 5 nm was sputtered (Sample A). The Al-O was prepared by plasma-oxidation of a 1.6-nm-thick Al layer. Sputtering power densities of Ag, Cu, NiFe were about 0.74, 1.48, and 1.48 W/cm^2, respectively. For a sample with a polycrystalline bottom electrode (Sample B), the same stacking and the same Al oxidation condition were used except for a thermally-oxidized Si substrate with Ta 3 nm/Cu 20 nm buffer layers and higher sputtering power density for every material used. Both samples were patterned into several

μm^2 using a micro-fabrication process including photolithography and Ar ion etching. Crystallographic orientation and surface morphology of films were examined using X-ray diffraction (XRD) and atomic force microscopy (AFM), respectively. TMR curves were measured at room temperature. The junction area was 30 ∞ 30 μm^2. Measurements were done by dc 4-probe method at a bias voltage of 1 mV.

3.2. Results and Discussion

The X-ray diffraction pattern for the bottom electrode of Sample A showed only fcc(111) peaks of NiFe and Cu, except for some peaks originated from the Si substrate. No peak was observed for Ag because it was very thin. The rocking curve measured for the NiFe(111) peak showed the full width at half-maximum (FWHM) of 0.80°, inferring a very small dispersion. The ϕ-scans of the {111} planes of NiFe, Cu and Si revealed that all layers grew epitaxially and that twin epitaxy existed in these films. The X-ray diffraction pattern for the bottom electrode of Sample B showed that the bottom electrode grown on a thermally oxidized Si had a textured polycrystalline structure with an fcc(111) preferred orientation.

Surface morphology of the bottom electrodes of Samples A and B are shown in Figs. 4(a) and 4(b), respectively. Image size of each sample is 500 nm ∞ 500 nm. Upper figures show cross sectional profiles along the lines in the corresponding images. Surface roughness of the epitaxial film ($R_a \cong 0.9$ nm) was slightly larger than that of the textured films ($R_a \cong 0.7$ nm). However, the cross section of the epitaxial film shows a more rounded and smooth surface in contrast to the textured film surface.

TMR ratios measured at as-deposited state were 32% for Sample A and 8% for Sample B. Fig. 5 shows TMR curves measured after annealing at 250°C. The resistance-area product of Samples A and B measured about 5.5 ∞ 10^5 $\Omega\mu m^2$ and 3.2 ∞ 10^5 $\Omega\mu m^2$, respectively. The TMR

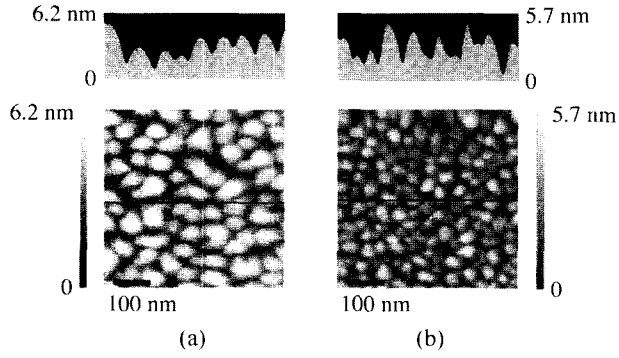

Fig. 4. AFM images of the surfaces of NiFe bottom electrodes in (a) Sample A (epitaxial) and (b) Sample B (textured).

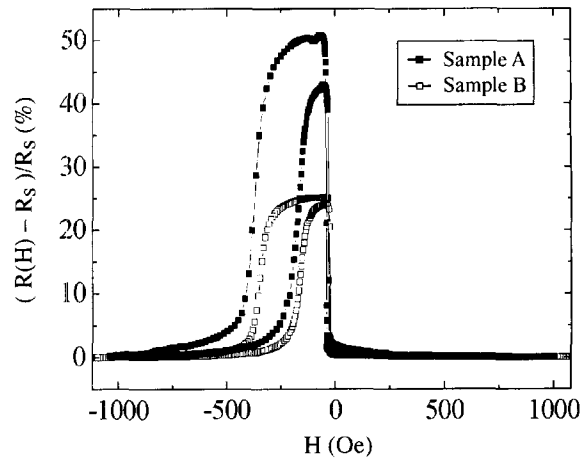

Fig. 5. TMR curves measured at RT for Samples A and B after annealing at 250°C.

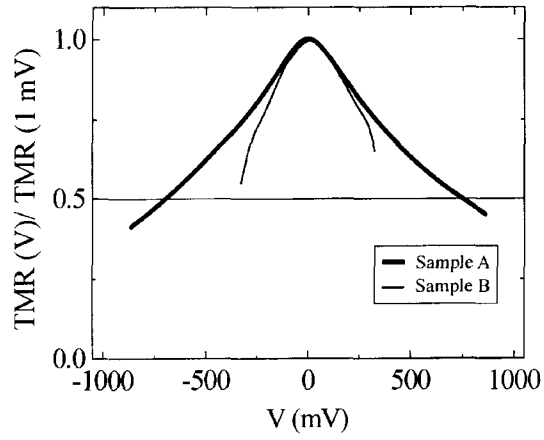

Fig. 6. Normalized TMR ratio versus dc bias voltage curves for Samples A and B measured at RT after annealing at 250°C.

ratio of Sample A was 51%, about two times larger than that of Sample B (27%).

It is also remarkable that the bias dependences of TMR ratio in the two samples differed greatly. Fig. 6 shows the normalized TMR ratio versus dc bias voltage curves measured at RT after annealing. Bold and solid lines represent results of Samples A and B, respectively. Both curves were obtained from the current (I)-dc bias voltage (V) curves measured at anti-parallel alignment (AP) and parallel alignment (P) of the magnetization of top and bottom electrodes. Positive bias was defined as the direction of current flow from the bottom electrode to the upper electrode. The V_{half}, the bias voltages at which the normalized TMR ratio becomes 0.5, of Sample A were +753 mV and –698 mV for positive and negative biases, respectively. On the other hand, the V_{half} of Sample B were estimated about 400 mV at both sides, which were much smaller than those of Sample A. The large difference of V_{half} between the two samples would be due to

different interfacial structures. In Sample B, the bottom FM electrode was composed of fcc(111) oriented grains that were randomly rotated in the film plane. Thus, there existed many high-angle grain boundaries in the polycrystalline NiFe layer. The metallic Al layer on the polycrystalline NiFe also had the same grain structure and included a number of grain boundaries as well. Due to the high angle grain boundaries of the metallic Al precursor layer, the Al-O layer would have decreased density after oxidation. Considering our previous work, oxygen atoms would penetrate into the NiFe bottom electrode along grain boundaries and create defects near the interface between the insulating layer and the NiFe layer. Therefore, the grain boundaries themselves would act as defects in spin-polarized electron tunneling. These defects must be one origin of strong bias dependence of TMR [22]. On the contrary, in the case of Sample A, layer structure was much denser than that of Sample B. It was reported that Al grows epitaxially on epitaxial NiFe, despite the large lattice parameter misfit of 12% [23]. Therefore, the absence of high angle grain boundaries in the Al metallic layer would lead to better uniformity of oxygen distribution in the insulating layer. Furthermore, over-oxidation along the grain boundaries of the NiFe would be suppressed, resulting in more homogeneous oxidation near the interface between the NiFe and Al-O layer. Consequently, in Sample A, there existed few defect states through which spin-independent tunneling occurs.

It should be noted that V_{half} values of Sample A were slightly asymmetric. This small asymmetry would be due to different interfacial structures between the upper and lower interfaces. However, analysis of an *I-V* curve for Sample A revealed nearly symmetric barrier heights at both interfaces. Therefore, further investigations with precise analysis, for example, inelastic electron tunnel spectroscopy (IETS), are necessary.

Fig. 7 shows Al-thickness dependences of TMR and resistance (R) ∞ junction area (A). Triangular dots represent the data of Sample A with a thicker Cu buffer layer (Sample A2, d_{Cu} = 100 nm) in which NiFe bottom electrodes showed more highly oriented structure. However, it also had larger roughness ($R_a \cong 1.3$ nm) than that of Sample A. When Al thickness exceeded 1 nm, the TMR ratio and RA slightly decreased with decreasing Al thickness. However, both values decreased rapidly at Al thickness of less than 1 nm. Non-uniform current flow due to rough interface and non-uniform thickness of the insulating layer would be responsible for these rapid decreases. Buffer layer stacking should be examined in order to suppress that roughness.

In summary, a great improvement in bias dependence of the TMR ratio was obtained in MTJs with an epitaxial FM bottom electrode. An insulator grown on the epitaxial bottom electrode would have fewer defects than the one on the textured bottom electrode. The result suggests that output signals of the devices based on MTJs, *e.g.* MRAM, can be enhanced very much by improving the insulating layer quality.

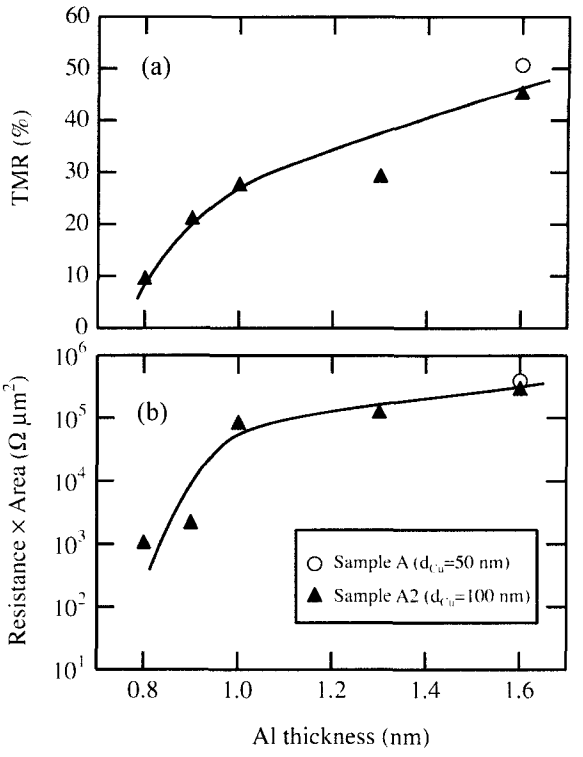

Fig. 7. Al thickness dependences of (a) TMR and (b) $R \infty A$ for samples with an epitaxially grown NiFe bottom electrode.

4. Hard mask fabrication for MRAM elements using FIB assisted selective CVD

Magnetic tunnel junctions (MTJs) [1, 2] have attracted much attention for the last few years because they have a high potential as a commercial device such as non-volatile magnetic random access memory (MARM) [3, 24] or highly sensitive magnetic sensor [25, 26]. Successful developments of prototype MRAMs have promoted a fundamental work for extending a capacity toward giga-bit order. In the fabrication of high density MRAMs, mask fabrication process is very important because uniformity of resistance, switching fields, and tunnel magnetoresistance (TMR) is deeply related to the shape of each bit pattern. To define a shape of bit patterns, an organic resist material is commonly used. They have many advantages in general production process, however, some difficulties exist in deep submicron scale. For a bit pattern of as small as 100

nm, very expensive lithography machines are necessary. A very thin resist layer is required for better resolution of bit patterns; however, the resist becomes weaker for ion etching process with decreasing its thickness. Variation of the shape of resist pattern results in wide distribution of resistance, TMR ratio and switching fields. In this work, carbon mask deposition using focused ion beam (FIB) assisted chemical vapor deposition (CVD) is examined as a mask fabrication process for submicron MTJ arrays. It is expected that carbon is mechanically hard but reacts with active oxygen. Basic deposition properties of the carbon masks are presented. Then, fabrication of MTJ arrays in 100 nm scale using carbon mask deposition technique is demonstrated.

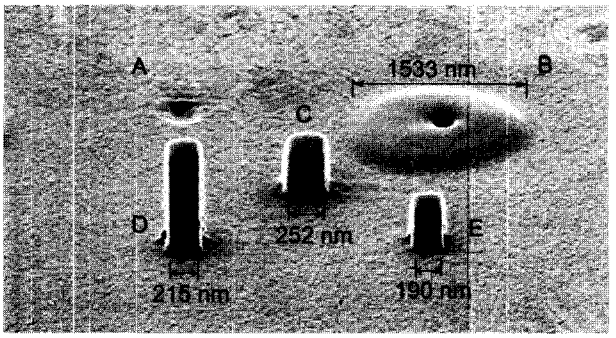

Fig. 8. SIM image of deposited carbon patterns fabricated using various aperture sizes. Aperture sizes used for A to D were 2000 μm, 300 μm, 150 μm, 75 μm, and 40 μm, respectively. The designed width and height were 200 nm and 1 mm, respectively. The actual pattern widths indicated in the image.

4.1. Experiments

The deposition experiments were carried out using SII model SMI9200 FIB machine. Ga ion beam was accelerated by a high voltage (30 kV) through an aperture. Probe current measured using a Faraday cup was 1-74 nA for aperture size of 40 μm-2 mm. In the smallest aperture size, the beam can be focused down to 7 nm in diameter. Gas source was phenanthrene ($C_{14}H_{10}$) powder, which was heated and kept at 339 K. The gas injected into the vacuum chamber through a nozzle, which was located near the sample surface during the deposition. The gaseous precursor was decomposed into solid carbon by reacting with energetic Ga ion beam. Etching rates were checked using an ECR etching machine with acceleration voltage of 400 V at an Ar pressure of 0.07 Pa and an oxygen pressure of 0.3 Pa. Incident angles were 0-15 degree away from film normal. Single layer Cu films and MTJ multilayers were prepared on thermally oxidized Si substrates using rf sputtering at Ar pressure of 0.07-0.2 Pa. The layer stacking of the multilayer was sub./Ta 5 nm/Ni-Fe 3 nm/Cu 20/Ir-Mn 10 nm/Ni-Fe 3 nm/Co-Fe 4 nm/Al-O/Co-Fe 3 nm/Ni-Fe 15 nm/Cr 5 nm/Au 20 nm. The Al-O layer was prepared using plasma oxidation of a 1.3-nm-thick Al film in a mixture of Ar and O_2. The top of the multilayer was covered by a resist 500 nm/Cu 20 nm double layer, on which carbon masks were deposited. A sample with carbon masks deposited directly on a MTJ film was also prepared. However, side walls of the carbon masks were covered by metals redeposited during Ar ion etching to define junction patterns. Oxygen ion etched the carbon surface but high walls of the metals redeposited remained at the pattern edges. The resist layer used was thick so that organic solvent dissolved the resist layer together with metals redeposited. The Cu layer on the resist layer was necessary to avoid a charge accumulation of Ga ions on the resist surface. Etching process was performed using an ECR etching machine with acceleration voltage of 400 V at an Ar pressure of 0.07 Pa and an oxygen pressure of 0.3 Pa. Incident angles were 0-15 degree away from film normal. Ar gas was used to etch the metal films and the Al-O film. Oxygen gas was used to remove thin carbon layers around patterns and to etch the thick resist layer.

4.2. Results and Discussion

Fig. 8 shows scanning ion microscopy (SIM) image of carbon patterns deposited on a Cu thin film with different aperture sizes. Designed width and height of the patterns were 200 nm and 1 μm, respectively. In the image, aperture size used for each pattern was indicated. Actual size and height depended significantly on the aperture size. For smaller aperture sizes, the patterns were cuboids. However, pattern shape deformed at aperture size more than 300 μm. Fig. 9 shows the aperture size dependences of probe currents and actual sizes of the carbon patterns. The probe current increased with increasing aperture size. According to the previous report, FIB assisted deposition can be described sa a competition between the ion induced precursor reaction and the removal of the precursor [27]. For smaller aperture sizes, where the deposition process is dominant, increaseing the beam intensity and diameter can increase both width and height of patterns. With increasing beam intensity, sputtering becomes dominant in inner side of the beam and deposition occurs in outer side of the beam. This effect caused the increase of the width and the decrease of the height of the carbon pattern. For the largest aperture size, thus, the largest beam intensity, the precursor was removed completely and the Cu surface was etched by sputtering. It is clear that the smallest aperture should be used to make precise patterns.

From a viewpoint of practical use, higher selectivity in

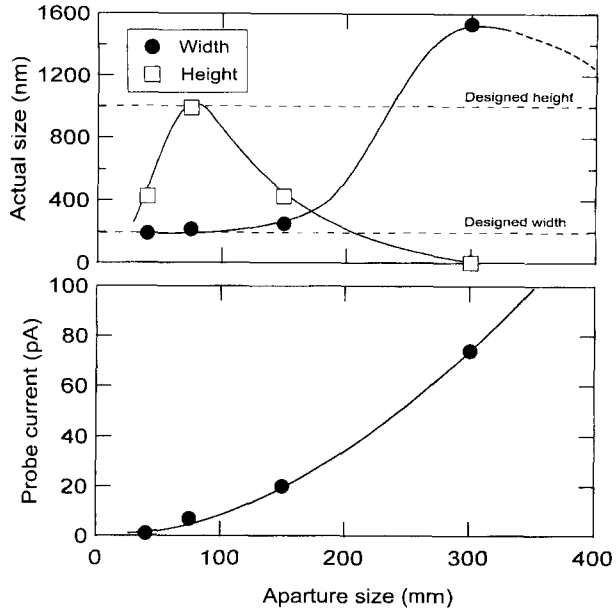

Fig. 9. Aperture size dependences of the actual size of carbon mask patterns (upper) and the probe current (lower).

Table 1. Comparison of etching rates (nm/s) between the carbon deposited and other metals

Gas	Carbon	Ni-Fe	Cu	Ta
Ar	0.19	0.14	0.37	0.05
O_2	0.34	0.03	0.05	<0.01

etching process is necessary for mask materials. Table 1 shows etching rates of the carbon deposited for Ar and oxygen ion etching. The carbon sample had an area of 15×15 μm^2. Etching rates of Ni-Fe, Cu, and Ta thin films, those are commonly used in MTJ in MRAM, are also listed for comparison. The carbon showed a lower etching rate for Ar ion etching. The rate was smaller than that of Cu and comparable with that of Ni-Fe. The etching rate of the carbon deposited for oxygen ion etching was much higher than those of other metals. These results indicate that the carbon deposited using this technique can be used as a mask in Ar ion etching process and can be removed by oxygen plasma with high selectivity.

Fig. 10 shows the variation of the actual width and height of the carbon mask patterns with various designed width. The designed width was varied between 10 nm and 500 nm, with keeping designed height at 1 μm. The smallest aperture of 40 μm in diameter was used. The actual width decreased linearly with decreasing of the designed width. The solid line along with closed circles crosses y-axis at about 30 nm, which is the smallest pattern width prepared in this condition. The actual height exhibited a maximum around the designed width of 90 nm, and decreased rapidly for smaller designed width.

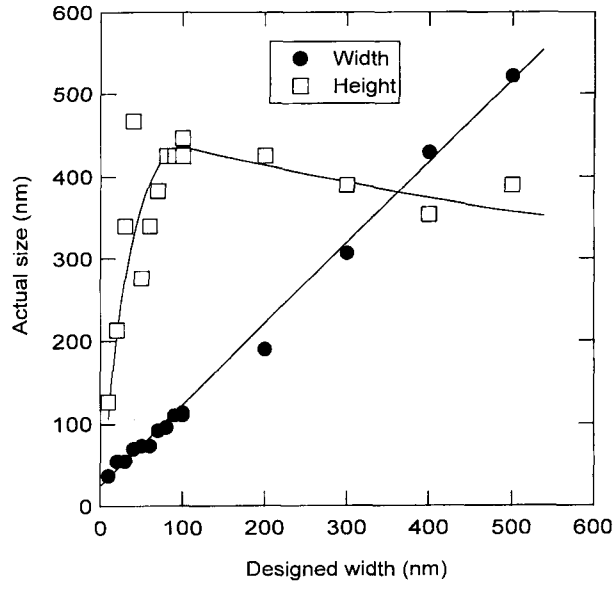

Fig. 10. Dependence of actual size of deposited carbon mask patterns on designed width. The designed height was kept at 1 μm.

Since the smallest pattern showed a conical shape, periphery was rounded remarkably. The minimum size for square pattern was about 80 nm. In this size, an aspect ratio (height/width) of the masks was more than 4. Here we should comment on deposition time. Deposition of one carbon mask with width of about 100 nm required about two seconds. It means that this technique is limited only for laboratory use.

Figs. 11(a) and (b) show SIM images of the carbon masks on a MTJ film/resist 500 nm/Cu 20 nm thin films. The images of bird view (a) and top view (b), were taken just after carbon deposition. The pattern sizes were 160 nm, 300 nm and 85 nm, for width, length and height, respectively. Size distribution in the pattern was quite small and well-defined rectangular shapes in the top view were obtained. Gray region around the patterns showed a continuous thin carbon layer formed by overlapping of the carbon deposition tails. Figs. 11(c) and (d) show SIM images observed after etching to define junction pattern. Heights of patterns increased because thick carbon/Cu/resist masks remained on the junctions. Top areas of the masks were smaller than the bottom areas. However, the top view of the patterns after etching (Fig. 11(d)) was identical to that observed before etching (Fig. 11(b)). Therefore, the junctions were defined into the same shape as that of the initial carbon mask patterns.

In summary, carbon deposition using FIB assisted selective CVD was examined as a mask fabrication process for small MTJ elements. The minimum size of the carbon mask with square pattern shape was about 80 nm,

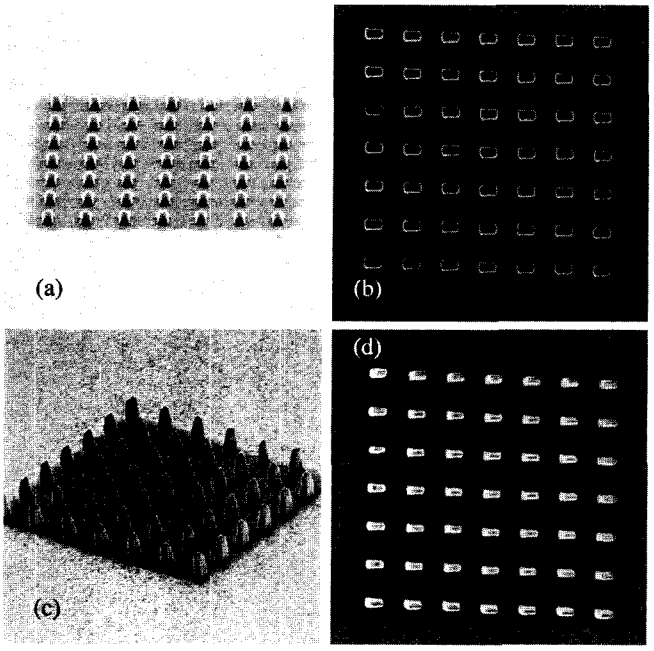

Fig. 11. SIM images of the carbon array deposited on the MTJ film observed before Ar ion etching (a), (b), and after etching to define junction patterns (c), (d). Patterned carbon/Cu/resist trilayers were used as mask patterns.

which corresponds to bit size in MRAM with giga bit capacity. Aspect ratio (height/width) of the masks more than 4 was achieved. The deposited carbon masks were as hard as Ni-Fe for Ar ion etching process and very soft for oxygen ion. Therefore, it is concluded that the carbon patterns prepared using FIB assisted selective CVD have a high potential as etching masks for MTJ arrays in 100 nm scale.

Acknowledgments

This study was supported by Grants-in-Aid for Scientific Research from the Ministry of Education, Culture, Sports, Science and Technology, CREST of JST, the SRC, and the Mitsubishi Foundation.

References

[1] T. Miyazaki and N. Tezuka, J. Magn. Magn. Mat. **139**, L231 (1995).
[2] J. S. Moodera, L. R. Kinder, T. M. Wong, and R. Meservey, Phys. Rev. Lett. **74**, 3273 (1995).
[3] S. S. P. Parkin, K. P. Roche, M. G. Samant, P. M. Rice, R. B. Beyers, R. E. Scheuerlein, E. J. O'Sullivan, S. L. Brown, J. Bucchigano, D. W. Abraham, Yu Lu M. Rooks, P. L. Trouilloud, R. A. Wanner, and W. J. Gallagher, J. Appl. Phys. **85**, 5828 (1999).
[4] M. Sato, H. Kikuchi, and K. Kobayashi, IEEE Trans. Magn. **35**, 946 (1999).
[5] X. F. Han, T. Daibou, M. Kamijo, K. Yaoita, H. Kubota, Y. Ando, and T. Miyazaki, Jpn. J. Appl. Phys. **39**, L439 (2000).
[6] S. Tehrani, J. M. Slaughter, E. Chen, M. Durlam, J. Shi, and M. DeHerrera, IEEE Trans. Magn. **35**, 2814 (1999).
[7] A. M. Bratkovsky, Appl. Phys. Lett. **72**, 2334 (1998).
[8] S. Zhang and P. M. Levy, Phys. Rev. Lett. **79**, 3744 (1997).
[9] J. Murai, Y. Ando, M. Kamijo, H. Kubota, and T. Miyazaki, Jpn. J. Appl. Phys. **38**, L1106 (1999).
[10] Y. Ando, J. Murai, H. Kubota, and T. Miyazaki, J. Appl. Phys. **87**, 5209 (2000).
[11] M. Hayashi, Y. Ando, and T. Miyazaki, Jpn. J. Appl. Phys. **40**, L1317 (2002).
[12] Y. Ando, M. Hayashi, S. Iura, K. Yaoita, C. C. Yu, H. Kubota, and T. Miyazaki, J. Phys. D: Appl. Phys. **35**, 2415 (2002).
[13] H. Itoh and J. Inoue, J. Magn. Magn. Mater. **226-230**, 930 (2001).
[14] M. Ichimura, T. Onogi, J. Hayakawa, and K. Itoh, Jpn. J. Appl. Phys. **40**, 4528 (2001).
[15] Y. Ando, H. Kubota, M. Hayashi, M. Kamijo, K. Yaoita, C. C. Yu, X. F. Han, and T. Miyazaki, Jpn. J. Appl. Phys. **39**, 5832 (2000).
[16] J. Fabian and S. Das Sarma, Phys. Rev. Lett. **83**, 1211 (1999).
[17] Y. Ando, M. Hayashi, M. Kamijo, H. Kubota, and T. Miyazaki, J. Magn. Magn. Mater. **226-230**, 924 (2001).
[18] A. E. T. Kuiper, M. F. Gillies, V. Kottler, G. W.'t Hooft, J. G. M. van Berkum, C. van der Marel, Y. Tamminga, and J. H. M. Snijders, J. Appl. Phys. **89**, 1965 (2001).
[19] S. Yuasa, T. Sato, E. Tamura, Y. Suzuki, H. Yamamori, K. Ando, and T. Katayama, Europhys. Lett. **52**, 344 (2000).
[20] M. Bowen, V. Cros, F. Petroff, A. Fert, C. Martínez Boubeta, J. L. Costa-Krämer, J. V. Anguita, A. Cebollada, F. Briones, J. M. de Teresa, L. Morellón, M. R. Ibarra, F. Güell, F. Peiró, and A. Cornet, Appl. Phys. Lett. **79**, 1655 (2001).
[21] H. Gong, M. Rao, D. N. Laughlin, and D. N. Lambeth, J. Appl. Phys. **85**, 5750 (1999).
[22] J. Zhang and R. M. White, J. Appl. Phys. **83**, 6512 (1998).
[23] Y. Li, S. X. Wang, G. Khanna, and B. M. Clemens, Thin Solid Films **381**, 160 (2001).
[24] S. Tehrani, B. Engel, J. M. Slaughter, E. Chen, M. DeHerrera, M. Derlam, P. Naji, R. Whig, J. Janesky, and J. Calder, IEEE Trans. Mag. **36**, 2752 (2000).
[25] S. Araki, K. Sato, T. Kagami, S. Sakurai, T. Uesugi, N. Kasahara, T. Kuwashima, N. Ohta, J. Sun, K. Nagai, S. Li, N. Hachisuka, H. Hatae, T. Kagotani, N. Takahashi, K. Ueda, and M. Matsuzaki, IEEE Trans. Magn. **38**, 72 (2002).
[26] E. Nakashio, J. Sugawara, S. Onoe, and S. Kumagai, J. Appl. Phys. **89**, 7356 (2001).
[27] Y. Fu, N. K. A. Bryan, and O. N. Shing, Sensors and Actuators A **88**, 58 (2001).